

$\lambda/20$ -Thick cavity for mimicking electromagnetically induced transparency at telecommunication wavelengths

Hua Lu¹,* Shouhao Shi, Dikun Li¹, Shuwen Bo, Jianxu Zhao, Dong Mao, and Jianlin Zhao¹*

Northwestern Polytechnical University, School of Physical Science and Technology, MOE Key Laboratory of Material Physics and Chemistry under Extraordinary Conditions, Key Laboratory of Light-Field Manipulation and Information Acquisition, Ministry of Industry and Information Technology, Shaanxi Key Laboratory of Optical Information Technology, Xi'an, China

Abstract Optical cavities play crucial roles in enhanced light–matter interaction, light control, and optical communications, but their dimensions are limited by the material property and operating wavelength. Ultrathin planar cavities are urgently in demand for large-area and integrated optical devices. However, extremely reducing the planar cavity dimension is a critical challenge, especially at telecommunication wavelengths. Herein, we demonstrate a type of ultrathin cavities based on large-area grown Bi_2Te_3 topological insulator (TI) nanofilms, which present distinct optical resonance in the near-infrared region. The result shows that the Bi_2Te_3 TI material presents ultrahigh refractive indices of >6 at telecommunication wavelengths. The cavity thickness can approach $1/20$ of the resonance wavelength, superior to those of planar cavities based on conventional Si and Ge high refractive index materials. Moreover, we observed an analog of the electromagnetically induced transparency (EIT) effect at telecommunication wavelengths by depositing the cavity on a photonic crystal. The EIT-like behavior is derived from the destructive interference coupling between the nanocavity resonance and Tamm plasmons. The spectral response depends on the nanocavity thickness, whose adjustment enables the generation of obvious Fano resonance. The experiments agree well with the simulations. This work will open a new door for ultrathin cavities and applications of TI materials in light control and devices.

Keywords: topological insulator; optical nanocavity; photonic crystal; electromagnetically induced transparency-like effect.

Received Oct. 27, 2023; revised manuscript received Feb. 20, 2024; accepted for publication Mar. 14, 2024; published online Apr. 3, 2024.

© The Authors. Published by SPIE and CLP under a Creative Commons Attribution 4.0 International License. Distribution or reproduction of this work in whole or in part requires full attribution of the original publication, including its DOI.

[DOI: [10.1117/1.AP.6.3.036001](https://doi.org/10.1117/1.AP.6.3.036001)]

1 Introduction

Optical cavities with excellent resonance and light confinement activities play crucial roles in light generation, modulation, detection, sensing, and storage for the realization of optical functional devices, integrations, and communications.^{1–5} The dimensions of optical cavities are generally limited by the material characteristics and operating wavelength. Metallic cavities enable light control and functionalities at visible and near-infrared ranges with the excitation of localized surface plasmon resonance on hundred-nanometer structures.^{6,7} Silicon (Si) dielectric particles

with several hundred nanometers can work as nanoresonators for functional devices at optical wavelengths.^{8,9} The complex geometries of metallic and dielectric cavities strongly depend on the precision fabrication process, limiting the fabrication of large-area devices. Ultrathin planar cavities play important roles in the large-area and integrated functional devices.^{10,11} High refractive index (HRI) materials attract considerable attention for achieving ultrathin nanocavities with strong light confinement and optical interference at the nanoscale.^{12,13} As conventional HRI materials, Si and germanium (Ge) semiconductors with refractive indices of ~ 3.47 and ~ 4.27 at 1550-nm wavelength have advanced the rapid developments of optical signal processing and communications.^{14,15} Ge material enables the realization of optical cavities with several hundred nanometers for

*Address all correspondence to Hua Lu, hualu@nwpu.edu.cn; Jianlin Zhao, jlzhao@nwpu.edu.cn

photodetection at the telecommunication band.¹⁶ The materials with higher refractive indices are in great demand for acquiring extremely thin cavities operating at telecommunication wavelengths. Different from traditional HRI semiconductors, topological insulators (TIs) as newly emerging quantum materials exhibit topologically protected conducting surface (or edge) and semiconducting bulk states.^{17–20} The state of matter with topological property was first reported in two-dimensional HgTe quantum wells.¹⁷ Subsequently, many three-dimensional (3D) materials with topological surface states were reported, such as Bi₂Te₃, Sb₂Te₃, Bi₂Se₃, and their compounds.^{19,20} Recently, topological materials have attracted broad attention in the fields of electronics, optics, and condensed matter physics because of their fantastic electronic and optical properties.^{18–24} Especially, 3D TI materials generally present the characteristic of HRI exceeding the refractive indices of Si and Ge at infrared wavelengths.^{21–23} TI materials will offer a promising prospect for achieving ultrathin optical cavities and their applications in novel optical effects and functional devices.

Electromagnetically induced transparency (EIT) is a counter-intuitive quantum interference effect occurring in atomic systems.²⁵ The EIT effect acts as an essential role in modern optical physics due to its significant applications in optical data storage, optical switching, and enhanced light nonlinearities.²⁶ Even so, the practical applications of atomic EIT are limited by the rigorous requirements of low temperature or stable gas lasing conditions.²⁷ Fortunately, the analogies to atomic EIT were observed in conventional optical cavities, such as photonic crystal cavities,²⁸ whispering-gallery-mode cavities,^{29,30} and metallic cavities.^{31–33} The EIT-like effects in coupled optical cavities can be used to realize advanced ultracompact devices, for instance, sensitive sensors,³² 3D rulers,³³ and optical switching.³⁴ Mimicking EIT in TI material-based cavities will not only enrich the formation mechanism of EIT-like effects but also advance the novel optical applications of TI materials, which, however, have not been demonstrated until now.

Herein, we reported a type of ultrathin planar cavities based on the large-area grown Bi₂Te₃ TI nanofilms, which possess obvious optical resonance in the near-infrared region. The experimental results demonstrate that the Bi₂Te₃ TI material presents ultrahigh refractive index at near-infrared wavelengths, contributing to the realization of optical cavities that are tens of nanometers in thickness. The TI material-based nanocavity thickness is $\sim 1/20$ of resonance wavelength ($\sim \lambda/20$), much thinner than those of cavities based on the conventional HRI Si and Ge materials. We also experimentally observed an analogy to atomic EIT at telecommunication wavelengths by depositing the nanocavity onto a one-dimensional (1D) photonic crystal. A transparency window distinctly appears in the original cavity-induced resonance absorption spectrum owing to the coupling between the nanocavity resonance and Tamm plasmons. The spectral profile relies on the cavity thickness and can evolve to an asymmetric Fano resonance line shape. The experimental results agree well with the simulations. This work will pave a new pathway for ultrathin optical cavities as well as the applications of TI materials in the mimicking of EIT and optoelectronic devices.

2 Results

Figure 1(a) shows the 3D diagram of the cavity with a TI material nanofilm coating on a metallic layer. To explore the optical properties, we fabricated the Bi₂Te₃ TI nanocavity by

using a magnetron sputtering (MS) technique (see Appendix). Figure 1(b) depicts an angle-tilted cross-sectional scanning electron microscopic (SEM) image of a nanocavity with the Bi₂Te₃ and silver nanofilms deposited on a SiO₂ substrate. d and t denote the thicknesses of Bi₂Te₃ and silver films, respectively. A 2-nm SiO₂ layer was deposited to isolate the silver and Bi₂Te₃ films for avoiding the formation of the Schottky barrier and charge transport.³⁵ The optical and top-view SEM images reveal the large area and good flatness properties of MS-grown Bi₂Te₃ nanofilms, respectively (see Fig. S1 in the Supplementary Material). Compared with the pulsed laser deposition, the MS technique enables the large-area growth of relatively flat Bi₂Te₃ films.³⁶ The MS method also presents the better flatness and higher growth rate for fabricating Bi₂Te₃ films when compared with the atomic layer deposition.³⁷ Figure 1(c) depicts the absorption spectrum of a 42-nm Bi₂Te₃ TI film on a 30-nm silver layer (i.e., $d = 42$ nm and $t = 30$ nm). The Bi₂Te₃ TI thickness can be clarified using the atomic force microscope (AFM) measurement (see Fig. S2 in the Supplementary Material). We measured the reflection, transmission, and absorption spectra of a TI nanocavity using a spectrophotometer (see Appendix). In Fig. S3 in the Supplementary Material, a distinct reflection dip appears at 1465-nm wavelength (i.e., $\lambda = 1465$ nm) for the cavity with a thickness of $\sim \lambda/20$, which is derived from the Fabry–Perot resonance in the asymmetric nanocavity. Here, the flat silver film with a large area can reflect a part of the incident light. The silver-reflected light will generate destructive interference with directly reflected light from the Bi₂Te₃ TI layer around the resonance wavelength.¹³ Thus, the reflection light of the cavity can be effectively suppressed. The cavity thickness of $\sim \lambda/20$ is ultrathin, according to the reported cavities.^{10,38,39} The optical loss of Bi₂Te₃ TI gives rise to strong resonance absorption at a broad wavelength range covering 1100 to 1800 nm, as depicted in Fig. 1(c). Moreover, we proposed to integrate the TI nanocavity onto a 1D photonic crystal, as can be seen in Fig. 1(d). The Bi₂Te₃ TI nanocavity was deposited on a photonic crystal with alternately stacked Ta₂O₅ and SiO₂ layers. The Ta₂O₅ and SiO₂ layers were fabricated using electron beam deposition. Figure 1(e) shows the angle-tilted cross-sectional SEM image of a fabricated TI nanocavity/photonic crystal structure. We can see that the photonic crystal has good uniformity with the periodic number $N = 16$. The thicknesses of Ta₂O₅ and SiO₂ layers are 182 and 260 nm, respectively (i.e., $d_t = 182$ nm and $d_s = 260$ nm). Figure 1(f) depicts the absorption spectrum of TI nanocavity/photonic crystal structure with $d = 42$ nm and $t = 30$ nm. A distinct narrow dip appears around 1550 nm wavelength in the absorption spectrum. Thus, the original broad absorption of TI nanocavity exhibits a transparency window at the telecommunication wavelength, which is analogous to the EIT effect in atomic systems.^{28,29} Meanwhile, we characterized the grown Bi₂Te₃ nanofilm using a transmission electron microscope (TEM). Figure 2(a) shows the TEM image of a grown 42-nm Bi₂Te₃ TI film transferred on the supporter of a copper microgrid (see Appendix and Note 1 in the Supplementary Material). The chemical composition of Bi₂Te₃ nanofilm can be confirmed using the energy-dispersive X-ray (EDX) measurement, which reveals the atomic ratio of Bi:Te $\approx 2:3$ (see Fig. S4 in the Supplementary Material). The good quality of Bi₂Te₃ can also be verified by the Raman shift spectrum (see Fig. S5 in the Supplementary Material).⁴⁰ Figure 2(b) depicts the selected area electron diffraction (SAED) pattern of

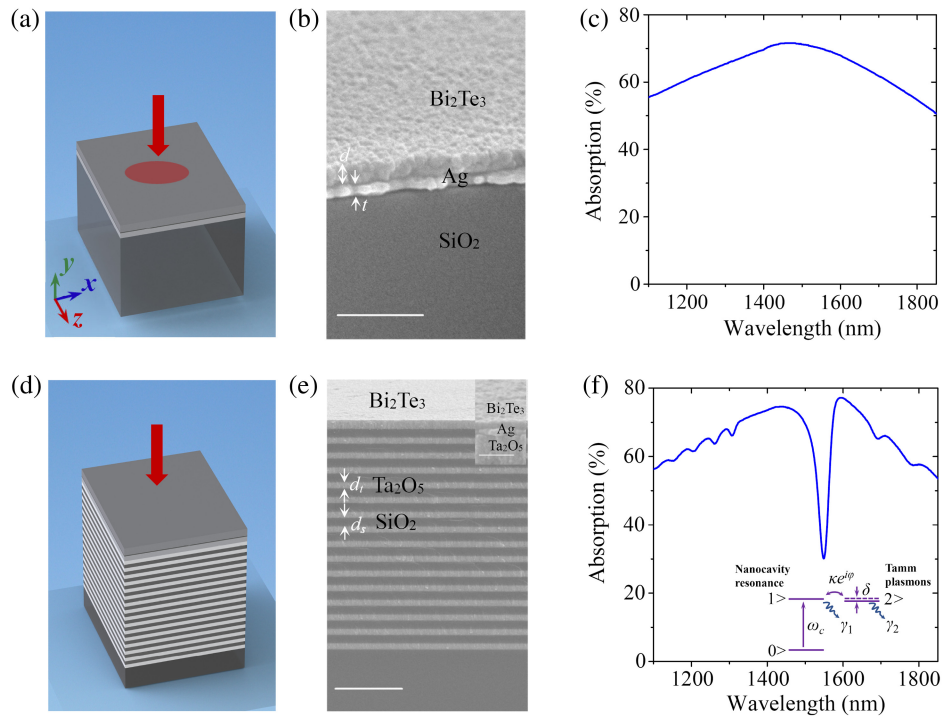


Fig. 1 TI structures and absorption spectra. (a) 3D diagram of the ultrathin nanocavity with a TI nanofilm coated on a metallic layer. (b) Angle-tilted cross-sectional SEM image of a Bi_2Te_3 TI nanocavity deposited on a SiO_2 substrate. The scale bar is 200 nm. Here, d and t are the thicknesses of Bi_2Te_3 and silver nanofilms, respectively. (c) Experimental measurement of the absorption spectrum of the nanocavity with a 42-nm Bi_2Te_3 film on a 30-nm silver layer (i.e., $d = 42$ nm and $t = 30$ nm). (d) 3D diagram of a TI nanocavity on a 1D photonic crystal. (e) Cross-sectional SEM image of a Bi_2Te_3 nanocavity on a photonic crystal with alternately stacked Ta_2O_5 and SiO_2 layers. Here, d_t and d_s are the thicknesses of Ta_2O_5 and SiO_2 layers, respectively. N is the periodic number. The scale bar is 2 μm . The inset shows the high-resolution SEM image of Bi_2Te_3 and silver films on the photonic crystal. The scale bar is 200 nm. (f) Measured absorption spectrum of the TI nanocavity/photonic crystal structure with $d_t = 182$ nm, $d_s = 260$ nm, $d = 42$ nm, $t = 30$ nm, and $N = 16$. The inset depicts a three-level system of the EIT-like effect. ω_c stands for the nanocavity resonant frequency. δ is the frequency detuning between the nanocavity resonance and Tamm plasmons in silver/photonic crystal structure. γ_1 and γ_2 are the decaying rates of nanocavity resonance and Tamm plasmons, respectively. $\kappa e^{i\varphi}$ is the complex coupling coefficient between the nanocavity resonance and Tamm plasmons with a phase retardation φ .

Bi_2Te_3 nanofilm, which corresponds to the rhombohedral Bi_2Te_3 phase.⁴¹ It also denotes that the MS-grown Bi_2Te_3 nanofilm presents the preferred growth orientation of (015). The high-resolution TEM (HRTEM) image in Fig. 2(c) illustrates multi-orientation atomic lattice arrangements in the Bi_2Te_3 nanofilm. The HRTEM image exhibits distinct fringes with some lattice spacing containing 0.321 and 0.220 nm, corresponding to the (015) and (110) planes of Bi_2Te_3 , respectively. The continuous rings of sharp diffraction pattern and atomic lattice arrangements reveal the polycrystalline nature of the Bi_2Te_3 nanofilm. We measured the optical constant of Bi_2Te_3 TI using a spectroscopic ellipsometer (see Appendix and Note 2 in the Supplementary Material). To differentiate the surface and bulk states, the ellipsometer-measured results can be fitted with the layer-on-bulk model.^{42,43} The surface and bulk were fitted with the Drude and Tauc–Lorentz dispersion relations, respectively.^{42–44} From Fig. 2(d), we can see that the fitted complex refractive indices agree well with the measurement. Figures 2(e) and 2(f) depict the complex refractive indices of surface and bulk for

the Bi_2Te_3 TI. For the surface, the extinction coefficient k is larger than the refractive index n at the wavelengths from 230 to 1930 nm, exhibiting metal-like characteristic. For the bulk, the refractive index can exceed 6.0 at the wavelengths of >1385 nm, which is much higher than the refractive indices of Si and Ge. The surface thickness was fitted as ~ 2.29 nm, approaching the estimated 2.5 nm for 3D TI.⁴⁵ The bandgap energy is ~ 0.21 eV, which is close to the reported bandgap (see Table S1 in the Supplementary Material).⁴⁶ The HRI property of our Bi_2Te_3 accords with the reported result of single-crystal Bi_2Te_3 film, even though there is a certain difference in the optical constants.⁴⁷ The ultrahigh refractive indices contribute to the ultrathin TI nanocavities at near-infrared range, similar to the Ge nanocavities at visible range.¹³ To our knowledge, this is the first report of a planar TI cavity with tens of nanometers in thickness at telecommunication wavelengths.

Subsequently, we measured the absorption spectra of TI nanocavities with different Bi_2Te_3 thicknesses. As shown in Fig. 3(a), the resonant absorption wavelength presents a redshift

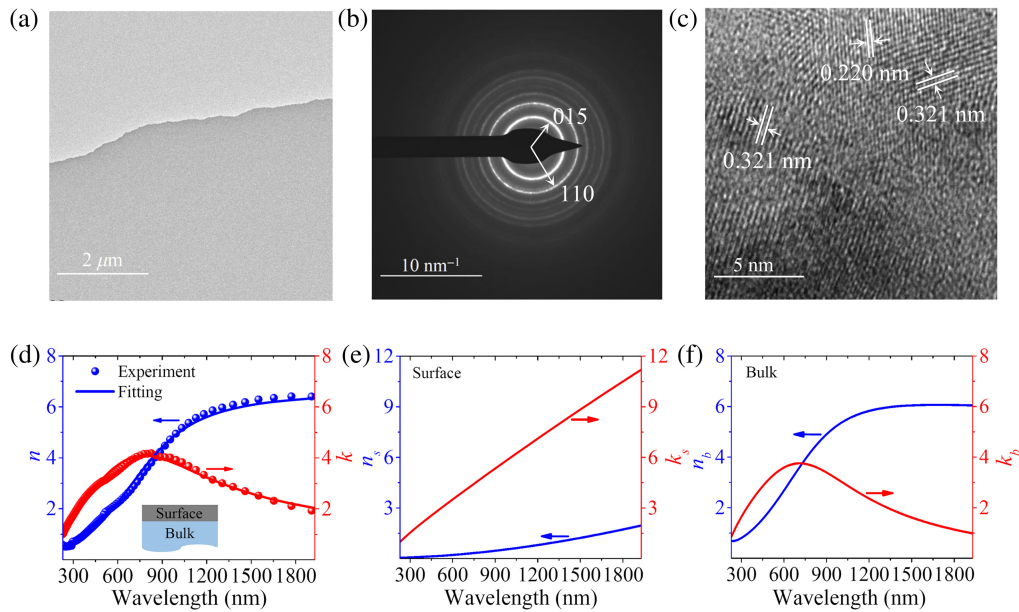


Fig. 2 Material characterization and optical constants of Bi_2Te_3 TI. (a) TEM image of a grown 42-nm Bi_2Te_3 TI film transferred on the supporter of a copper microgrid. (b) SAED pattern of the Bi_2Te_3 nanofilm. (c) HRTEM image of the Bi_2Te_3 nanofilm. (d) Ellipsometer-measured (circles) and fitted (curves) refractive indices and extinction coefficients of Bi_2Te_3 TI at the wavelengths from 230 to 1930 nm. (e), (f) Fitted refractive indices and extinction coefficients of Bi_2Te_3 TI surface and bulk states with the layer-on-bulk model [the inset in panel (d)].

in the near-infrared region as d increases from 30 to 52 nm. Simultaneously, the absorption peak possesses an obvious rise. To verify the experimental results, the absorption spectra were theoretically calculated using the transfer matrix method (see Fig. S6 and Note 3 in the [Supplementary Material](#)).⁴⁸ In the calculations, we employed the measured complex refractive indices of the Bi_2Te_3 TI surface and bulk in Figs. 2(e) and 2(f) as well as the measured optical constants of silver film in Fig. S7 in the [Supplementary Material](#). As depicted in Fig. 3(b), there exists a nearly linear relation between the absorption peak wavelength and Bi_2Te_3 TI thickness. As mentioned above, the TI nanocavity thickness is $\sim 1/20$ of the resonance wavelength. Moreover, we simulated the spectral response and field distributions of the TI nanocavities using the finite-difference time-domain (FDTD) method (see [Appendix](#)). We can see that the experimental measurements agree well with the theoretical and simulation results. Figure 3(c) depicts the intensity distribution of the magnetic field in the TI nanocavity at the absorption peak wavelength. It shows that the magnetic field is confined and distinctly enhanced in the nanocavity. As shown in Fig. 2(d), there are large extinction coefficients for the Bi_2Te_3 TI at near-infrared wavelengths, which means that the TI nanocavity possesses high optical loss. Thus, the Fabry–Perot resonance in the asymmetric cavity can give rise to relatively strong light absorption in the near-infrared region.¹³ The absorption ratio between the Bi_2Te_3 TI and silver nanofilms is $\sim 13:1$, revealing that the light absorption mainly stems from the Bi_2Te_3 TI nanofilm [see Fig. S8(a) in the [Supplementary Material](#)]. From Fig. S8(b) in the [Supplementary Material](#), we can see that the TI bulk dominates in the light absorption of Bi_2Te_3 nanofilm, and the surface layers induce a slight redshift of the resonance absorption peak. Moreover, we deposited a 30-nm silver

film on the photonic crystal and measured the spectral response (see Fig. S9 in the [Supplementary Material](#)). The result demonstrates that there exists a narrow reflection dip and an absorption peak at the wavelength of ~ 1560 nm, which results from the formation of Tamm plasmons in the silver/photonic crystal multilayer. Both the Bi_2Te_3 /silver and silver/photonic crystal structures present relatively strong light absorption at the wavelengths from 1545 to 1580 nm. Intuitively, the TI nanocavity/photonic crystal structure would present stronger absorption at these wavelengths, but a distinct transparency window appears around 1550 nm in the absorption spectrum, as shown in Fig. 1(f). The generation of reflection dips in the silver/photonic crystal structure is similar to the Tamm plasmon response in previous structures.^{49–51} But, the appearance of absorption dips in the Bi_2Te_3 /silver/photonic crystal structure is fundamentally different from the spectral response (reflection dips) in the Tamm plasmon structures, even with a poly(vinyl alcohol) layer on the metal.^{50,51} As mentioned above, this counterintuitive phenomenon can be regarded as an analogy to the EIT effect in atomic systems.^{31,32,52} It can be analyzed with a prototype three-level model, as depicted in the inset of Fig. 1(f). In the model, $|1\rangle$ and $|2\rangle$ stand for the upper states, and $|0\rangle$ denotes the ground state. The light impinges on the Bi_2Te_3 nanofilm and excites the resonance in the TI nanocavity, which is analogous to the transition from $|0\rangle$ to $|1\rangle$.^{31,53} Tamm plasmons can be generated by the evanescent field of nanocavity resonance, which will couple with each other. The coupling between the nanocavity resonance and Tamm plasmons is analogous to the transition between the states $|1\rangle$ and $|2\rangle$. The two possible transition processes $|0\rangle \rightarrow |1\rangle \rightarrow |2\rangle \rightarrow |1\rangle$ and $|0\rangle \rightarrow |1\rangle$ will form the destructive interference. The interference coupling contributes to the appearance of a narrow

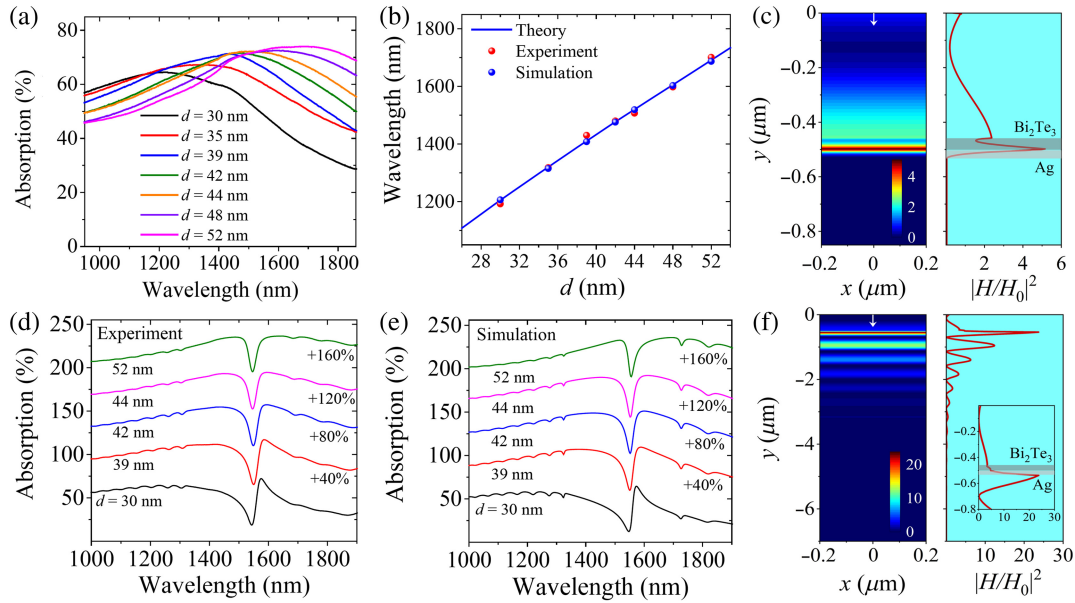


Fig. 3 TI thickness-dependent nanocavity resonance and induced transparency. (a) Experimentally measured absorption spectra of the TI nanocavities on the SiO_2 substrate with different Bi_2Te_3 film thicknesses d when $t = 30$ nm. (b) Corresponding resonance wavelengths of the TI nanocavity with different d . The curve, red circles, and blue circles denote the theoretical, experimental, and simulation results, respectively. (c) Corresponding magnetic field distribution of the TI nanocavity with a 42-nm Bi_2Te_3 film (i.e., $d = 42$ nm) at the absorption peak wavelength. (d), (e) Measured and simulated absorption spectra of the TI nanocavity/photonic crystal structures with different d when $t = 30$ nm. (f) Corresponding magnetic field distribution of the TI nanocavity/photonic crystal structure with a 42-nm Bi_2Te_3 film at the absorption dip wavelength.

transparency window in the broad absorption peak. Therefore, the EIT-like effect is generated due to the coupling between the Fabry–Perot resonance in the planar TI cavity and Tamm plasmons in the silver/photonic crystal structure. This is different from the generation mechanism of EIT-like transmission in previous plasmonic structures, e.g., the dielectric waveguide with silver nanoparticles.⁵⁴ In Fig. 1(f), we can see some small grooves in the absorption spectrum around the transparency window. The small grooves correspond to the transmission peaks of the multilayer structure, which originate from the constructive interference at the output interface, not the EIT-like effect. We measured the spectral response of TI nanocavity/photonic crystal structures with different Bi_2Te_3 thicknesses d when $t = 30$ nm. From Fig. 3(d), we can see that the EIT-like spectral profile is dependent on d . The EIT-like spectrum distinctly appears as d ranges from 42 to 52 nm, which denotes that the EIT-like behavior is robust to the small fabrication deviation of Bi_2Te_3 thickness. However, an obviously asymmetric Fano-type line shape can be generated when $d = 30$ nm. The formation of Fano resonance can be derived from the coherent interference between a quasi-continuum state (broadly spectral nanocavity off-resonance) and a discrete excited state (narrowly spectral Tamm plasmons). The numerical simulations are in excellent agreement with the experimental results, as depicted in Fig. 3(e). Figure 3(f) shows the magnetic field distribution of the TI nanocavity/photonic crystal structure with a 42-nm Bi_2Te_3 film at the absorption dip wavelength (i.e., 1550 nm). It is found that Tamm plasmons between the silver film and photonic crystal can be excited with a distinct field enhancement. It verifies the nanocavity coupling-induced excitation of Tamm plasmons.

Interestingly, the coupling-induced Tamm plasmons can effectively reduce the strong light absorption in traditional Tamm plasmon systems, which will be beneficial for reinforcing light–matter interactions. Finally, we studied the dependence of the EIT-like spectrum on the silver film thickness t in the TI nanocavity/photonic crystal structure, as shown in Fig. 4(a). The theoretical calculations illustrate that the induced transparency window becomes narrower and shallower with the increase of t . To verify it, we fabricated the TI nanocavity/photonic crystal structures with $t = 15, 30, 40,$ and 50 nm when $d = 44$ nm and measured their absorption spectra.

As depicted in Fig. 4(b), the experimental results verify the theoretical prediction of spectral evolution. To clarify the mechanism of the EIT-like effect, we theoretically fitted the measured absorption spectra with the two-coupled-oscillator (TCO) model (see Appendix). The results show that the decaying rate γ_1 of oscillator 1 (TI nanocavity) slightly changes as the Bi_2Te_3 TI thickness varies from 15 to 50 nm. γ_1 is $\sim 1.02 \times 10^{15}$ rad/s when $t = 30$ nm. The decaying rate γ_2 of oscillator 2 (silver/photonic crystal structure) slowly increases with t and can approach 0.85×10^{13} rad/s when $t = 30$ nm. The coupling strength κ between oscillators 1 and 2 rapidly decreases as t increases. κ reaches 5.5×10^{13} rad/s when $t = 30$ nm, which is much less than the threshold coupling strength κ_T [$\kappa_T = (\gamma_1 - \gamma_2)/4 = 5.06 \times 10^{14}$ rad/s]. Therefore, the coupling between the nanocavity resonance and Tamm plasmons is located in the weak-driving regime when $t = 30$ nm.²⁹ The coupling phase retardation φ approaches π in the TI nanocavity/photonic crystal structures with different t (see Fig. S10 in the Supplementary Material), verifying the destructive

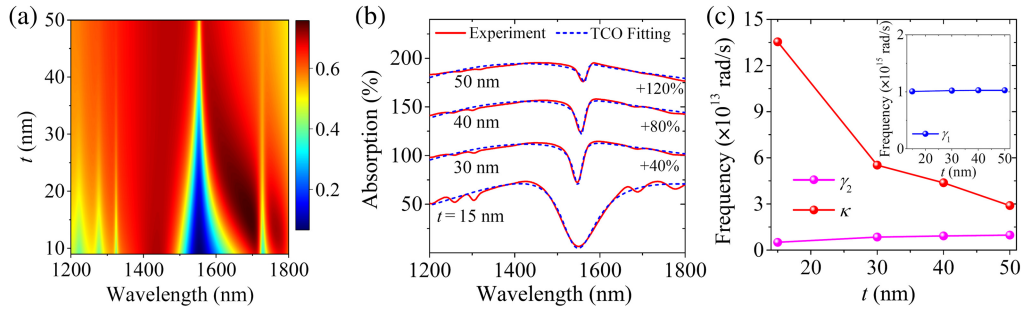


Fig. 4 EIT-like response with different silver film thicknesses. (a) Theoretical evolution of absorption spectrum from the TI nanocavity/photonic crystal structures with different silver film thicknesses t when $d = 44$ nm. (b) Measured (solid curves) and fitted (dashed curves) absorption spectra of the TI nanocavity/photonic crystal structures with different t when $d = 44$ nm. Here, the experimentally measured spectra were fitted with the TCO model. (c) Fitted decaying rates γ_2 and coupling strengths κ in the TCO model with different t . The inset shows the corresponding decaying rates γ_1 .

interference between the nanocavity resonance and Tamm plasmons. Because the coupling strength satisfies the criterion $\kappa < \kappa_T$, the observed transparency windows in our systems are attributed to the EIT-like effect with the existence of large γ_1 and small γ_2 even when t declines to 15 nm, as depicted in Fig. 4(c). Thus, the EIT-like response can be achieved in the TI nanocavity/photonic crystal structure with a Bi_2Te_3 film thickness of $\sim\lambda/25$. The absorption dip can approach a low value of 6% at the 1550-nm wavelength when $t = 15$ nm (see Fig. S11 in the [Supplementary Material](#)). It means that the EIT-like effect can effectively bypass the optical loss in the structure with a small silver thickness.

3 Discussion

The Bi_2Te_3 TI possesses an ultrahigh refractive index at near-infrared wavelengths, much exceeding the conventional HRI Si and Ge semiconductors [see Fig. 2(d)]. The ultrahigh refractive index of Bi_2Te_3 TI enables the realization of planar cavities with tens of nanometers in thickness, which can find promising applications in light-matter interaction, for instance, infrared optoelectronic conversion. From Fig. 1(c) and Fig. S3 in the [Supplementary Material](#), we can see that the TI cavity with a 42-nm Bi_2Te_3 film presents an ultrabroad resonance absorption of light with high efficiency of $>50\%$ at the wavelengths from 970 to 1850 nm. The nanocavities can effectively break the absorption limit of 50% for ultrathin free-standing film at near-infrared range.⁵⁵ As shown in Fig. S8 in the [Supplementary Material](#), the light absorption mainly stems from the Bi_2Te_3 TI nanofilm with a narrow-bandgap semiconducting property. The absorption ratio between the TI and silver nanofilms is $\sim 13:1$ around the resonance wavelength. The Bi_2Te_3 TI cavities will contribute to the high-efficiency, broad-spectrum, ultrathin, and large-area near-infrared optoelectronic devices, e.g., telecommunication band photodetectors.

From Fig. 3(b), we can see that the resonance wavelength presents a linear redshift with the increasing Bi_2Te_3 TI thickness. The resonance wavelength is ~ 20 times as large as the TI nanocavity thickness ($\sim 0.05\lambda$), which is more remarkable than the subwavelength-thin (0.13λ) layer of Ge nanostructures.⁵⁵ This property also enables the precision monitoring of nanofilm thickness in the deposition process.¹³ To achieve this kind of optical cavities, the thicknesses of Bi_2Te_3 TI are much thinner

than those of HRI Si and Ge semiconductors (see Fig. S12 in the [Supplementary Material](#)). For example, the Bi_2Te_3 TI thickness is $\sim 53\%$ (64%) of Si (Ge) thickness for optical resonance at the 1550-nm wavelength. Thus, the thickness of the Bi_2Te_3 TI cavity can be improved by 34% (24.5%) compared with that of the Si (Ge) cavity. Moreover, the nanocavities may find applications in ultrathin structures for wavefront shaping, similar to Si metasurfaces.⁸

The TI nanocavities will offer new building blocks for realizing novel optical effects. Herein, we have innovatively integrated the TI nanocavity onto a photonic crystal with alternately stacked Ta_2O_5 and SiO_2 layers. Interestingly, an analogy to the atomic EIT effect has been observed at telecommunication wavelengths. This EIT-like behavior is attributed to the destructive interference coupling between the resonance in TI nanocavity and Tamm plasmons in silver/photonic crystal structure. Compared with the conventional materials, the Bi_2Te_3 TI with relatively high refractive index and extinction coefficient has the specific advantage for the generation of the EIT-like effect in this system (see Fig. S13 in the [Supplementary Material](#)). Besides the nanocavity thicknesses, the EIT-like response is also dependent on the incident light angle. From Fig. S14 in the [Supplementary Material](#), we can see that the induced transparency wavelength exhibits a blueshift with the increase of incident light angle. This stems from the identical shift of the Tamm plasmon wavelength by altering the incident light angle. The shifted wavelength of s-polarized light is different from that of p-polarized light, which stems from the energy splitting between the s- and p-polarized Tamm states.⁴⁹ The adjustment of the incident light angle offers an effective way for dynamic tunability of the induced transparency window. The induced transparency spectrum can also be tuned by controlling the polarization of light at oblique incidence, as shown in Fig. S14(f) in the [Supplementary Material](#). This kind of cavity structures based on planar multilayers can effectively avoid the fabrication process and area limitations of the structures based on dielectric or metallic nanoparticles for the generation of EIT-like effects. The EIT-like effect presents good robustness to the alteration of the environmental refractive index (see Fig. S15 in the [Supplementary Material](#)). The TI nanocavity also enables the formation of EIT-like behavior by integrating with the thin Ge and silver layers (see Fig. S16 in the [Supplementary](#)

Material). The thickness can be effectively improved when compared with the Ge-based cavity. This work will open a new door for ultrathin optical cavities and promote the applications of TIs in light control and optical functional devices.

4 Appendix: Methods

4.1 Fabrication

The Bi_2Te_3 TI and silver nanofilms were prepared by the MS deposition technique. The Bi_2Te_3 film was deposited using radio-frequency (RF) sputtering with a pressure of 0.9 Pa and power of 70 W. The silver film was deposited using the direct current sputtering with a pressure of 0.6 Pa and power of 50 W. The feasible grown area can be set as $4\text{ cm} \times 4\text{ cm}$ for the flat nanofilms in our MS deposition. The 2-nm SiO_2 layer was deposited by employing the RF sputtering with a pressure of 1 Pa and power of 100 W. The flowing Ar (100 sccm) was employed as the sputtering gas. The 1D photonic crystal with alternately stacked Ta_2O_5 and SiO_2 layers was prepared on the polished SiO_2 substrate (Beijing Dream Material Technology Co., Ltd.) through electron beam deposition.

4.2 Characterizations and Measurements

The surface flatness of grown Bi_2Te_3 TI nanofilm was characterized using the commercial SEM equipment (FEI Verios G4) and AFM system (Bruker Dimension FastScan). The AFM system was also used to test the thicknesses of deposited films. The material morphology of Bi_2Te_3 TI nanofilm was characterized through the SAED pattern and HRTEM image, which were measured using the TEM equipment (FEI Talos F200X) with a voltage of 200 kV. The Raman spectrum of Bi_2Te_3 TI was measured using a confocal microspectrometer (WITec Alpha300R) with a 532-nm laser. The complex refractive index of Bi_2Te_3 TI in the optical region was tested by employing a spectroscopic ellipsometer (HORIBA UVISSEL Plus) with a 70-deg incident light angle. The absorption, reflection, and transmission spectra of fabricated samples were measured using a spectrophotometer (Hitachi UH5700).

4.3 Simulations

To verify the experimental results, we employed the FDTD method to numerically simulate the optical spectra and field distributions of TI nanocavity and TI nanocavity/photonic crystal structures.⁵⁶ In FDTD simulations, the bottom and top of structures were set as the perfectly matched layer absorbing boundary conditions. The other sides of computational space were set as the periodic boundary conditions. The non-uniform mesh was utilized in the y -axis direction to fully consider the influence of each layer. The mesh size of the Bi_2Te_3 TI surface layer was set as 0.3 nm. The maximum mesh size of other layers was 5 nm. The absorption spectra of the entire structures were achieved with $A = 1 - |P_r/P_i| - |P_t/P_i|$, where P_r , P_t , and P_i denote the powers of reflected, transmitted, and incident light, respectively. The complex refractive indices of Bi_2Te_3 TI surface and bulk were set as the measured values in Figs. 2(e) and 2(f). The measured complex refractive index of MS-deposited silver film was used in the simulations (see Fig. S7 in the [Supplementary Material](#)). The refractive indices of SiO_2 and Ta_2O_5 were set as 1.44 and 2.058 at the wavelengths of interest,

respectively.^{57,58} The refractive indices of Si and Ge in the simulations come from the experimental data.^{59,60}

4.4 Theory

To clarify the mechanism of the EIT-like effect in the TI nanocavity/photonic crystal structures, we theoretically studied the EIT-like spectra with the TCO model.^{31,53} As shown in Fig. 1(c), the resonant mode in the TI nanocavity (i.e., oscillator 1) can be generated when the light is incident on the Bi_2Te_3 TI nanofilm. Tamm plasmons in silver/photonic crystal structure (i.e., oscillator 2) can be excited by the resonant coupling of TI nanocavity. As depicted in the inset of Fig. 1(f), ω_c stands for the resonant frequency of oscillator 1. δ is the frequency detuning between oscillators 1 and 2. γ_1 and γ_2 are the decaying rates of oscillators 1 and 2, respectively. $\kappa e^{i\varphi}$ is the complex coupling coefficient between the two oscillators with a coupling phase retardation φ . When $|\omega - \omega_c| \ll \omega_c$, $\gamma_2 \ll \gamma_1 \ll \omega_c$, and $|\delta| \ll \gamma_1$, the light absorption in the entire structure can be described as

$$A(\omega) = \text{Im} \left\{ \frac{f(\omega - \omega_c + \delta + i\gamma_2/2)}{(\kappa e^{i\varphi})^2 - (\omega - \omega_c + i\gamma_1/2)(\omega - \omega_c + \delta + i\gamma_2/2)} \right\}, \quad (1)$$

where $A(\omega)$ is the imaginary part of the solution for the coupled differential equations of the two oscillators.^{31,53} f is an amplitude coefficient. According to Eq. (1), we can fit the experimentally measured absorption spectra to extract the related physical parameters. As shown in Fig. 4(b), the fitting curves are well consistent with the experimental results, verifying the feasibility of the theoretical model.

Disclosures

The authors declare no competing interests.

Code and Data Availability

All the data that support the findings of this study are available from the corresponding authors upon reasonable request.

Author Contributions

H.L. conceived the idea; carried out the theoretical calculations, numerical simulations, sample fabrications, and characterizations; analyzed results; drew the figures; and wrote the manuscript text. S.H.S. participated in the fabrications of Bi_2Te_3 and silver films. D.K.L. took part in the sample preparation for TEM measurements. S.W.B. and D.K.L. conducted the experimental measurement of optical spectra. J.X.Z. participated in the fitting of complex refractive index for Bi_2Te_3 TI. D.M. and J.L.Z. discussed the results and helped to promote the manuscript presentation. All authors substantially contributed to the manuscript.

Acknowledgments

This work was supported by the National Key R&D Program of China (Grant No. 2022YFA1404800), the National Natural Science Foundation of China (Grant Nos. 11974283, 61705186, and 11774290), the Natural Science Basic Research Plan in Shaanxi Province of China (Grant No. 2020JM-13), the ‘‘Double First-Class’’ Construction Fund Project (Grant No. 0206022GH0202), and the Fundamental Research Funds

for the Central Universities (Grant No. D5000220175). The authors thank the Analytical & Testing Center of Northwestern Polytechnical University (NPU) for the TEM, AFM, SEM, Raman, and EDX measurements.

References

1. L. Yang et al., "Topological-cavity surface-emitting laser," *Nat. Photonics* **16**(4), 279–283 (2022).
2. H. Wang et al., "Towards optimal single-photon sources from polarized microcavities," *Nat. Photonics* **13**(11), 770–775 (2019).
3. J. Ni et al., "Multidimensional phase singularities in nanophotonics," *Science* **374**(6566), eabj0039 (2021).
4. X. Zhang et al., "Symmetry-breaking-induced nonlinear optics at a microcavity surface," *Nat. Photonics* **13**(1), 21–24 (2019).
5. T. Shi et al., "Planar chiral metasurfaces with maximal and tunable chiroptical response driven by bound states in the continuum," *Nat. Commun.* **13**, 4111 (2022).
6. H. Altug et al., "Advances and applications of nanophotonic biosensors," *Nat. Nanotechnol.* **17**(1), 5–16 (2022).
7. C. Chi et al., "Selectively steering photon spin angular momentum via electron-induced optical spin Hall effect," *Sci. Adv.* **7**(18), eabf8011 (2021).
8. I. Staude and J. Schilling, "Metamaterial-inspired silicon nanophotonics," *Nat. Photonics* **11**(5), 274–284 (2017).
9. T. Liu et al., "High-efficiency optical frequency mixing in an all-dielectric metasurface enabled by multiple bound states in the continuum," *Phys. Rev. B* **107**, 075441 (2023).
10. A. Shaltout et al., "Ultrathin and multicolour optical cavities with embedded metasurfaces," *Nat. Commun.* **9**, 2673 (2018).
11. J. Wu et al., "Graphene oxide for integrated photonics and flat optics," *Adv. Mater.* **33**(3), 2006415 (2021).
12. M. L. Brongersma et al., "Light management for photovoltaics using high-index nanostructures," *Nat. Mater.* **13**(5), 451–460 (2014).
13. M. A. Kats et al., "Nanometre optical coatings based on strong interference effects in highly absorbing media," *Nat. Mater.* **12**(1), 20–24 (2013).
14. X. Gan et al., "Chip-integrated ultrafast graphene photodetector with high responsivity," *Nat. Photonics* **7**(11), 883–887 (2013).
15. S. Lischke et al., "Ultra-fast germanium photodiode with 3-dB bandwidth of 265 GHz," *Nat. Photonics* **15**(12), 925–931 (2021).
16. W. Hu et al., "Germanium/perovskite heterostructure for high-performance and broadband photodetector from visible to infrared telecommunication band," *Light Sci. Appl.* **8**, 106 (2019).
17. M. König et al., "Quantum spin Hall insulator state in HgTe quantum wells," *Science* **318**(5851), 766–770 (2007).
18. H. Krishnamoorthy et al., "Topological insulator metamaterials," *Chem. Rev.* **123**(8), 4416–4442 (2023).
19. H. Zhang et al., "Topological insulators in Bi_2Se_3 , Bi_2Te_3 and Sb_2Te_3 with a single Dirac cone on the surface," *Nat. Phys.* **5**(6), 438–442 (2009).
20. D. Kong et al., "Ambipolar field effect in the ternary topological insulator $(\text{Bi}_x\text{Sb}_{1-x})_2\text{Te}_3$ by composition tuning," *Nat. Nanotechnol.* **6**(11), 705–709 (2011).
21. H. Lu et al., "Topological insulator plasmonics and enhanced light-matter interactions," in *Plasmon-Enhanced Light-Matter Interactions*, P. Yu, H. Xu, and Z. Wang, Eds., pp. 89–116, Springer International Publishing, Cham (2022).
22. H. Lu et al., "Magnetic plasmon resonances in nanostructured topological insulators for strongly enhanced light-MoS₂ interactions," *Light Sci. Appl.* **9**, 191 (2020).
23. J. Yin et al., "Plasmonics of topological insulators at optical frequencies," *NPG Asia Mater.* **9**(8), e425 (2017).
24. X. Sun et al., "Topological insulator metamaterial with giant circular photogalvanic effect," *Sci. Adv.* **7**, eabe5748 (2021).
25. K. J. Boller et al., "Observation of electromagnetically induced transparency," *Phys. Rev. Lett.* **66**(20), 2593–2596 (1991).
26. T. F. Krauss, "Why do we need slow light?" *Nat. Photonics* **2**(8), 448–450 (2008).
27. L. V. Hau et al., "Light speed reduction to 17 metres per second in an ultracold atomic gas," *Nature* **397**(6720), 594–598 (1999).
28. N. Caselli et al., "Generalized Fano lineshapes reveal exceptional points in photonic molecules," *Nat. Commun.* **9**, 396 (2018).
29. B. Peng et al., "What is and what is not electromagnetically induced transparency in whispering-gallery microcavities," *Nat. Commun.* **5**, 5082 (2014).
30. C. Wang et al., "Electromagnetically induced transparency at a chiral exceptional point," *Nat. Phys.* **16**(3), 334–340 (2020).
31. N. Liu et al., "Plasmonic analogue of electromagnetically induced transparency at the Drude damping limit," *Nat. Mater.* **8**, 758–762 (2009).
32. N. Liu et al., "Planar metamaterial analogue of electromagnetically induced transparency for plasmonic sensing," *Nano Lett.* **10**(4), 1103–1107 (2010).
33. N. Liu et al., "Three-dimensional plasmon rulers," *Science* **332**(6036), 1407–1410 (2011).
34. T. Kim et al., "Electrically tunable slow light using graphene metamaterials," *ACS Photonics* **5**(5), 1800–1807 (2018).
35. M. Sabarinathan et al., "*n*-type to *p*-type transition of electrical conduction in silver (Ag)-modified Bi_2Te_3 nanosheets," *J. Electron. Mater.* **51**(12), 7275–7282 (2022).
36. A. Bailini et al., "Pulsed laser deposition of Bi_2Te_3 thermoelectric films," *Appl. Surf. Sci.* **254**(4), 1249–1254 (2007).
37. M. Rusek et al., "Bismuth amides as promising ALD precursors for Bi_2Te_3 films," *J. Cryst. Growth* **470**, 128–134 (2017).
38. K. Sreekanth et al., "Biosensing with the singular phase of an ultrathin metal-dielectric nanophotonic cavity," *Nat. Commun.* **9**, 369 (2018).
39. S. N. Chowdhury et al., "Wide-range angle-sensitive plasmonic color printing on lossy-resonator substrates," *Adv. Opt. Mater.* **12**(4), 2301678 (2024).
40. L. Goncalves et al., "Optimization of thermoelectric properties on Bi_2Te_3 thin films deposited by thermal co-evaporation," *Thin Solid Films* **518**(10), 2816–2821 (2010).
41. V. Y. Kolosov and A. A. Yushkov, "Microstructures in thin Bi_2Te_3 films according to transmission electron microscopy," *AIP Conf. Proc.* **2313**, 030019 (2020).
42. J. Y. Ou et al., "Ultraviolet and visible range plasmonics in the topological insulator $\text{Bi}_{1.5}\text{Sb}_{0.5}\text{Te}_{1.8}\text{Se}_{1.2}$," *Nat. Commun.* **5**, 5139 (2014).
43. H. Lu et al., " Sb_2Te_3 topological insulator: surface plasmon resonance and application in refractive index monitoring," *Nanoscale* **11**(11), 4759–4766 (2019).
44. G. Jellison and F. Modine, "Parameterization of the optical functions of amorphous materials in the interband region," *Appl. Phys. Lett.* **69**(3), 371–373 (1996).
45. B. Xia et al., "Indications of surface-dominated transport in single crystalline nanoflake devices of topological insulator $\text{Bi}_{1.5}\text{Sb}_{0.5}\text{Te}_{1.8}\text{Se}_{1.2}$," *Phys. Rev. B* **87**(8), 085442 (2013).
46. Y. Lin et al., "Thermocatalytic hydrogen peroxide generation and environmental disinfection by Bi_2Te_3 nanoplates," *Nat. Commun.* **12**, 180 (2021).
47. N. Krishnamoorthy et al., "Infrared dielectric metamaterials from high refractive index chalcogenides," *Nat. Commun.* **11**, 1692 (2020).
48. H. Lu et al., "Nearly perfect absorption of light in monolayer molybdenum disulfide supported by multilayer structures," *Opt. Express* **25**(18), 21630–21636 (2017).
49. B. I. Afinogenov et al., "Ultrafast all-optical light control with Tamm plasmons in photonic nanostructures," *ACS Photonics* **6**(4), 844–850 (2019).
50. R. Badugu and J. R. Lakowicz, "Tamm state-coupled emission: effect of probe location and emission wavelength," *J. Phys. Chem. C* **118**(37), 21558–21571 (2014).

51. R. Badugu et al., “Radiative decay engineering 7: Tamm state-coupled emission using a hybrid plasmonic-photonic structure,” *Anal. Biochem.* **445**, 1–13 (2014).
52. S. Xiao et al., “Active modulation of electromagnetically induced transparency analogue in terahertz hybrid metal-graphene metamaterials,” *Carbon* **126**, 271 (2018).
53. L. Mao et al., “Reversible switching of electromagnetically induced transparency in phase change metasurfaces,” *Adv. Photonics* **2**(5), 056004 (2020).
54. Y. He et al., “Plasmon induced transparency in a dielectric waveguide,” *Appl. Phys. Lett.* **99**(4), 043113 (2011).
55. J. Tian et al., “Near-infrared super-absorbing all-dielectric metasurface based on single-layer germanium nanostructures,” *Laser Photonics Rev.* **12**(9), 1800076 (2018).
56. A. Taflove and S. Hagness, *Computational Electrodynamics: The Finite-Difference Time-Domain Method*, 2nd ed., Artech House, Boston, MA (2000).
57. T. J. Bright et al., “Infrared optical properties of amorphous and nanocrystalline Ta₂O₅ thin films,” *J. Appl. Phys.* **114**(8), 083515 (2013).
58. J. Kischkat et al., “Mid-infrared optical properties of thin films of aluminum oxide, titanium dioxide, silicon dioxide, aluminum nitride, and silicon nitride,” *Appl. Opt.* **51**(28), 6789–6798 (2012).
59. E. Palik, *Handbook of Optical Constants of Solids*, Academic Press (1998).
60. M. J. Weber, *Handbook of Optical materials*, CRC Press, Boca Raton (2003).

Hua Lu is as a professor at Northwestern Polytechnical University in China. He received his PhD from the Chinese Academy of Sciences. He was a postdoc fellow at Swinburne University of Technology in Australia, and then joined Northwestern Polytechnical University in 2015. His current research interest is focused on nanophotonics, plasmonics, and nanomaterials. To date, he has published more than 100 articles in professional journals, including *Light Sci. Appl.*, *Adv. Photon.*, *Laser Photon. Rev.*, and *Small*, with citation counts of >6400. He received the 13th Shaanxi Youth Science and Technology Award (2020) and was continuously selected as Elsevier’s Highly Cited Chinese Researcher (2021–2023).

Jianlin Zhao is a chief scientist at Northwestern Polytechnical University and the director of MOE Key Laboratory of Material Physics and Chemistry under Extraordinary Conditions. He has been selected as a fellow of the Chinese Optical Society and the executive editor-in-chief of *Acta Optica Sinica*. His research interests include micro-/nanophotonics, light-field manipulation, digital holography, and optical fiber sensing. To date, he has published three textbooks (sole author) and more than 500 articles in professional journals, including *Science*, *Nat. Mater.*, *Adv. Mater.*, *Light Sci. Appl.*, and *Nat. Commun.*, with citation counts of >13,000. He was continuously selected as Elsevier’s Highly Cited Chinese Researcher (2021–2023).

Biographies of the other authors are not available.